Journal Name

Dynamic Article Links ►

Cite this: DOI: 10.1039/c0xx00000x

www.rsc.org/xxxxxx

ARTICLE TYPE

Facile Bottom-Up Synthesis of Graphene Nanofragments and Nanoribbons by Thermal Polymerization of Pentacenes

Yosuke Ishii,[a] Hayong Song,[a] Hidenori Kato,[b] Masashige Takatori[b] and Shinji Kawasaki*[a]

Received (in XXX, XXX) Xth XXXXXXXXX 20XX, Accepted Xth XXXXXXXXX 20XX

DOI: 10.1039/b000000x

To prepare nanosize graphene-like molecules of a defined structure (defined-width graphene nanoribbons or nanofragments) by a simple bottom-up method, thermal polymerization reactions of pentacenes were investigated. By optimizing heat treatment temperature and initial precursor weight, long-length fused pentacene molecules were successfully obtained at least up to octamer (n = 8). Here, the degree of polymerization was much larger than that of previously known polymerized pentacene systems (n = 2, 3). The structural and physical properties of the obtained fused pentacenes were characterized by Raman spectroscopy, X-ray diffraction, and photoluminescent spectroscopy. The fused pentacene system, examined using density functional theory calculations, was found to have unique electronic and magnetic structures originating from its characteristic size and edge structure. In addition, we performed detailed mass spectroscopic analysis that examined the fusing mechanism.

Introduction

Since the groundbreaking report by Geim and Novoselov[1] in 2004, graphene, which is a single layer of graphite, has attracted much attention.[2-5] With its unique physical and electronic structure, graphene is expected to be used in next-generation electronic devices,[6] sensors,[7-10] transparent electrodes,[11, 12] and energy storage devices.[13-16]

Although graphene samples prepared by the mechanical cleaving method proposed by Geim and Novenselov[1] have a significant advantage in terms of quality, the quantity of samples obtained by this method is considerably limited. Therefore, in recent years, enormous effort has been invested to synthesize large amounts of graphene. High-quality single- and few-layered graphene sheets have successfully been grown by the decomposition of silicon carbide,[17-20] chemical vapor deposition on single and polycrystal transition metals,[21-23] and pulsed laser deposition.[24, 25] However, controlling graphene morphology (size and edge structure) with these top-down methods is still a challenge. Because theoretical studies have predicted that the electronic and magnetic properties of graphenes are greatly affected by their size and edge structure,[26-30] control of their morphology is essential for graphene applications.

To this end, chemical syntheses based on the bottom-up strategy should be a promising approach because we can control graphene morphology by designing appropriate precursors. For example, Simpson *et al.* reported the synthesis route for a $C_{222}H_{42}$ molecule with 91 benzene rings using the cyclodehydrogenation reaction of a $C_{222}H_{150}$ polyphenylene dendritic precursor.[31] Although this approach could be used for large-scale production of graphene-like molecules of a defined structure, such an organic synthetic route requires many stepwise reactions.

Another bottom-up approach for graphene synthesis is using direct dehydrogenation reaction of commonly available polycyclic aromatic hydrocarbon (PAH) precursors. For example, Talyzin *et al.* recently reported the thermal polymerization of coronene ($C_{24}H_{12}$) molecules.[32] However, the exact molecular size and structure of the polymerized products were not well determined probably because of the large variety of product molecules. Because coronene has an isotropic zigzag edge structure, we cannot control growth direction and morphology. A promising method for controlling graphene morphology with PAH precursors is a template method that uses single-walled carbon nanotubes (SWCNTs) as a reactor.[33–36] Long-length and width-defined graphene nanoribbons (GNRs) can be synthesized by this method. However, the extraction of GNRs from SWCNTs is still a difficult task. To synthesize GNRs without using a structural template, we should use PAH precursors with an anisotropic edge structure. Recently, Cai *et al.* reported a method of fabricating GNRs from PAH molecules having -Br groups at the zigzag edge.[37] Here, the -Br groups were used as structural directing milestones for graphene growth. Moreover, some of the acenes (PAH molecules composed of linearly fused benzene rings) seem to polymerize in a definite direction without any special functional groups. For instance, a fusing reaction of pentacene (**1**, $C_{22}H_{14}$) molecules was reported by Roberson *et al.*[38] By heating pentacenes under inert gas flow, a dehydrogenation condensation reaction occurs at the zigzag edge and a mixture of a pentacene dimer (**2**, peripentacene) and trimer (**3**, trisperipentacene) can be obtained. By developing this method, long-length GNRs of pentacene width can be prepared as shown in Scheme 1.

Cite this: DOI: 10.1039/c0xx00000x

www.rsc.org/xxxxxx

ARTICLE TYPE

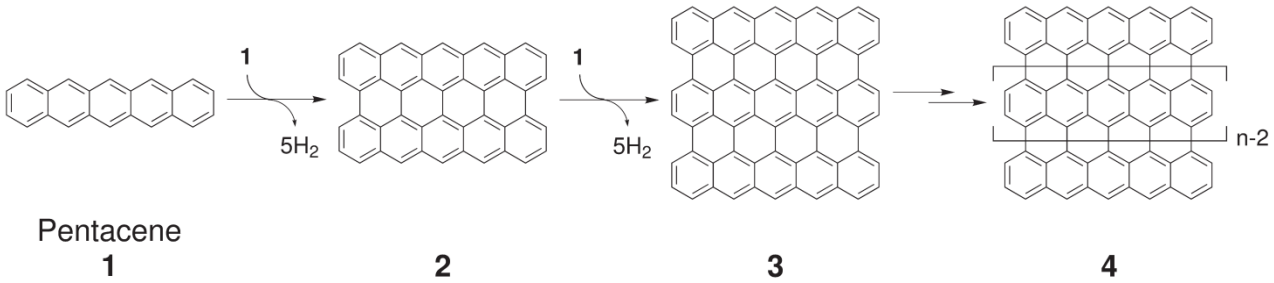

Scheme 1 Bottom-up synthesis approach for GNRs using pentacene as a precursor

Recently, we performed spectroscopic characterization of fused pentacene molecules and found that the obtained materials have a unique electronic structure similar to graphene sheets even in the dimer or trimer.[39] Therefore, we expect that fused pentacenes can be used as model materials for graphene nanofragments (GNFs). However, fused pentacenes larger than tetramer have not been synthesized yet. In addition, the obtained materials contained a wide variety of byproducts in addition to the proposed GNR molecules. This can be clearly seen in the mass spectra in our previous report.[39] To achieve efficient synthesis and produce larger sizes of fused pentacenes, the experimental conditions must be refined.

Here, we report the correlation between the preparation conditions and detailed molecular compositions of fused pentacenes. By optimizing the fusing condition, we have successfully obtained large fused pentacenes up to at least octamer. Note that this degree of polymerization is much higher than that previously reported.[38, 39] Furthermore, the relationship between the length of fused pentacenes and their electronic structures is discussed. The fusing mechanisms are also addressed in this paper.

Experimental and computational methods

We performed the fusing treatment of pentacenes as follows. First, 30 mg of commercially available pentacene powder (Kuroganekasei Co. Ltd., endothermic peak measured by a differential scanning calorimeter: 416 °C) was sealed in an evacuated quartz tube (<2 Pa, inner volume ~20 cm^3). The tube was heated to the target temperature at a rate of 5 °C min^{-1} and maintained at the temperature for 10 h. The target temperature was varied at 275, 300, 310, 325, 340, 350, 375, 400, and 425 °C. Here, vaporization of initial pentacene seemed to occur at around the target temperature and the fusing reaction should produce hydrogen gas. For the experiment at 325 °C, we varied initial pentacene weight (15, 30, and 100 mg) to check the effect of hydrogen gas pressure on the fusing reaction. To remove unreacted pentacene and byproducts, the samples recovered after the reactions were washed with toluene in an ultrasonic bath and filtered repeatedly until the solvent's color became clear and colorless. For convenience, the obtained insoluble products (fused pentacene, FP) were designated as FP-*W*-*T*, where *W* and *T* represent initial pentacene weight (mg) and reaction target temperature (°C), respectively. In addition, to address the reaction mechanism, experiments using 6.13-dyhydropentacene (DHP) mixed with initial pentacene were also performed. In these experiments, target temperature was fixed at 325 °C. The obtained materials were designated as PW_1-DHPW_2, where W_1 and W_2 represent initial pentacene weight (mg) and initial DHP weight (mg), respectively. The detailed experimental methods are mentioned in ESI†.

To examine the electronic structure of polymerized pentacenes, first-principles calculations were performed. Structural optimizations and energy calculations of fused pentacene molecules were performed by density functional theory (DFT) calculations using Gaussian 03 software[40]. Here, we used the B3LYP exchange-correlation hybrid functional[41] with Dunning's double-zeta correlation consistent basis sets[42] (cc-pVDZ). The electronic structures of a graphene nanoribbon having infinite length and the pentacene monomer units were calculated with the ABINIT code[43, 44]. Here, the Perdew-Wang 92 exchange-correlation functional[45] within local density approximation with the projected augmented wave method[46, 47] was employed for the calculation. The unit cell structure (slab model) of the graphene nanoribbon that was used for the calculation is shown in Fig. S1. We employed a tetragonal unit cell and the direction of the nanoribbon's axis was set to *b*. Each nanoribbon was separated by a ~1.5 nm vacuum layer in the *a*- and *c*-axes directions to suppress interaction between the layers. A 2 × 16 × 4 Monkhorst-Pack k-point mesh sampling was used for Brillouin zone integration. Moreover, the plane wave cutoff was set to 30 Ha (816 eV).

Results and discussion

Figure 1 shows the laser desorption/ionization time-of-flight (LDI-TOF) mass spectra of the obtained materials as a function of heat treatment temperature. Except in the case of 310 °C, well-separated strong peak bands (marked with down-pointing triangles in Fig. 1) were clearly observed at around m/z = 550, 810, 1090, 1360, 1630, 1900, and 2160. These positions are in agreement with the molecular weights of polymerized pentacenes.

Some readers may think that these bands originated from noncovalently bonded pentacene clusters generated in the ionization process of mass spectroscopic measurements. However, this idea should be dismissed because the specific peak positions of the observed spectra (Fig. 2) are quite different from those of the cluster ions. The observed peak positions cannot be explained without the existence of covalently bonded pentacenes.

The detailed mass spectra of each band are shown in Fig. 2. In the case of the pentacene dimer region shown in Fig. 2A(a), the most intense peak position (m/z = 546.13) shows good agreement with the monoisotopic mass of peripentacene (**2**, $C_{44}H_{18}$, m = 546.14). Although peak intensities were not always highest in each band region, straightly grown pentacene polymers (**4**, $C_{22n}H_{4n+10}$, n = 1, 2, 3⋯) were detected at least until octamer (n = 8) in this study. This degree of polymerization was much higher than that in previous reports (n = 2, 3).[38, 39] LDI-TOF mass spectra of the obtained materials as a function of initial pentacene weight are shown in Fig. S2†. As shown in Figs. 1 and S2†, the most suitable reaction temperature and initial pentacene weight for obtaining large fused products were found to be 325 °C and 30 mg, respectively, for a 20 cm^3 vacuum tube. Under these conditions, about 9 mg of the fused product was recovered after the purification process. The relation between the size of polymerized molecules and above mentioned experimental parameters (i.e. reaction temperature, and initial pentacene weight) will be discussed later in this paper.

To characterize the structural properties of the obtained materials, Raman spectroscopy and X-ray diffraction (XRD) measurements were performed. As mentioned in our previous paper, in addition to the well-known G-band (in-plane carbon atom vibration mode of the graphene layer) located at around 1600 cm^{-1}, a fused pentacene system should show unique Raman peak features due to hydrogen atom vibrations at the molecular edge.[39] The Raman spectrum of the FP-30-325 sample is shown in Fig. S3(a)†. In the spectrum, small peaks were observed at 1239, 1346, and 1460 cm^{-1} in addition to a large peak at ~1600 cm^{-1}. The positions of these small peaks agree well with those of theoretically predicted pentacene-based GNFs [see Figs. S3(b)–(d)†]. A typical XRD pattern of fused pentacene (FP-30-325) is shown in Fig. S4†. We found that the XRD patterns of the fused pentacene samples were completely different from that of initial pentacene.[39] As shown in Fig. S4†, only some broad peak features (halo pattern) were observed in the FP-30-325 sample. This result means that the fused pentacenes existed in an amorphous state. The largest halo peak was observed at 2θ = 25.6°. This peak probably represents the π–π stacking feature of graphene layers, and we evaluated the average layer distance as 0.348 nm. Interestingly, the estimated layer distance is considerably larger than that of the well-known graphite crystal. Having a larger interlayer distance is favourable for suppressing interactions between adjacent layers.

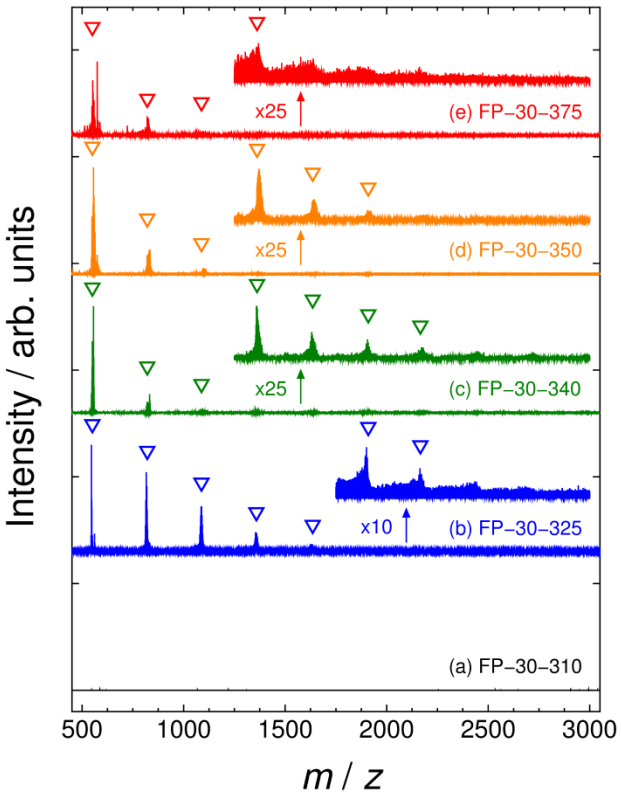

Fig. 1 LDI-TOF mass spectra of the samples (a) FP-30-310, (b) FP-30-325, (c) FP-30-340, (d) FP-30-350, and (e) FP-30-375.

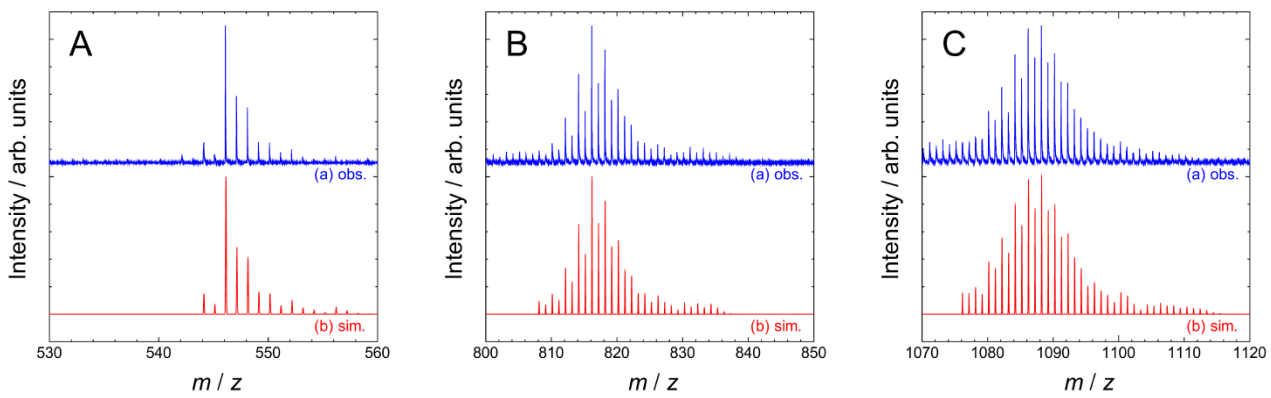

Fig. 2 Detailed LDI-TOF mass spectra of the FP-30-325 sample. In addition to the observed spectra (a), simulated patterns (b) that considered isotope distribution are also shown in the graph. In the spectrum simulation, the molecular compositions in the (A) dimer, (B) trimer, and (C) tetramer regions were set to $C_{44}H_{16}$:$C_{44}H_{18}$:$C_{44}H_{20}$:$C_{44}H_{22}$:$C_{44}H_{24}$:$C_{44}H_{26}$:$C_{44}H_{28}$ = 15:100:30:12:9:2:5, $C_{66}H_{16}$:$C_{66}H_{18}$:$C_{66}H_{20}$:$C_{66}H_{22}$:$C_{66}H_{24}$:$C_{66}H_{26}$:$C_{66}H_{28}$:$C_{66}H_{30}$:$C_{66}H_{32}$:$C_{66}H_{34}$:$C_{66}H_{36}$:$C_{66}H_{38}$:$C_{66}H_{40}$:$C_{66}H_{42}$ = 11:14:35:37:100:70:44:21:12:13:4:8:7:7, and $C_{88}H_{20}$:$C_{88}H_{22}$:$C_{88}H_{24}$:$C_{88}H_{26}$:$C_{88}H_{28}$:$C_{88}H_{30}$:$C_{88}H_{32}$:$C_{88}H_{34}$:$C_{88}H_{36}$:$C_{88}H_{38}$:$C_{88}H_{40}$: $C_{88}H_{42}$:$C_{88}H_{44}$:$C_{88}H_{46}$:$C_{88}H_{48}$:$C_{88}H_{50}$:$C_{88}H_{52}$:$C_{88}H_{54}$:$C_{88}H_{56}$ =

22:18:46:58:86:100:96:68:50:22:21:9:18:2: 8:8:5:5:3, respectively. Here, to allow comparison with experimental spectra, the calculated patterns were broadened by a Gaussian function with 0.07 mass unit of a full width at half maximum.

Regarding the size of the conjugated carbon system, the width of a pentacene monomer unit is about 1.2 nm. On the other hand, the length of a fused pentacene is expressed as 0.43*n* [nm]. Therefore, the obtained materials are considered to be nanosize graphene fragments. Here, note that such small-width GNRs or GNFs cannot be prepared by well-known top-down techniques such as electron beam lithography.[48] Such small-size molecules should show unique electronic and magnetic structures due to the so-called quantum confinement or edge effect.[28-32]

To understand the electronic and magnetic structures of the fused pentacene system, we performed theoretical calculations. The electronic densities of states (DOSs) and spin densities of the straightly grown fused pentacenes (**4**, n = 1, 2, 3, 4, and 5) are summarized in Fig. 3. As is well known, the electronic structure of bulk graphene is described as a zero-gap semiconductor (semi-metal); the unique electronic structure of graphene is represented by so-called Dirac cones, and its valence and conduction bands are crossed at the Fermi level (E_F).[49] Therefore, the DOSs of bulk graphene sheets linearly increase with distance from E_F. As can be seen in Fig. 3, the DOSs of the fused pentacene system (n > 2) were symmetrically dispersed from E_F just like the above-mentioned graphene's DOS feature (see dashed red lines in Fig. 3(e)). However, the fused pentacenes have an additional DOS feature that can be observed in bulk graphene; some discrete energy levels (marked with red arrows in Fig. 3(e)) just like the van Hove singularities in SWCNTs are also observed in the fused pentacene system. Interestingly, the positions of the discrete energy levels were almost independent of the polymerized length (n) of pentacenes (see Fig. 3). These discrete energy levels were maintained even in the pentacene-based GNR having infinite length (see Fig. S5[†]). From the DFT calculation of the fused oligomers, we found that the fused pentacene molecules have some band gap. For example, the HOMO–LUMO gap of the pentakisperipentacene (**4**, n = 5) was estimated to be 1.45 eV. Having such a band gap feature is a great advantage for semiconductor applications. Because the band gap of an ideal graphene sheet is zero, logic devices composed of ideal large-area graphene cannot be switched off; therefore, bulk graphene sheets are unsuitable for such applications.[50, 51] Furthermore, because the obtained fused molecules were of nanoscale, the molecules may be used for extremely small-size electronic circuit systems. Thus, fused pentacenes should be promising candidates for next-generation nanoelectronic materials.

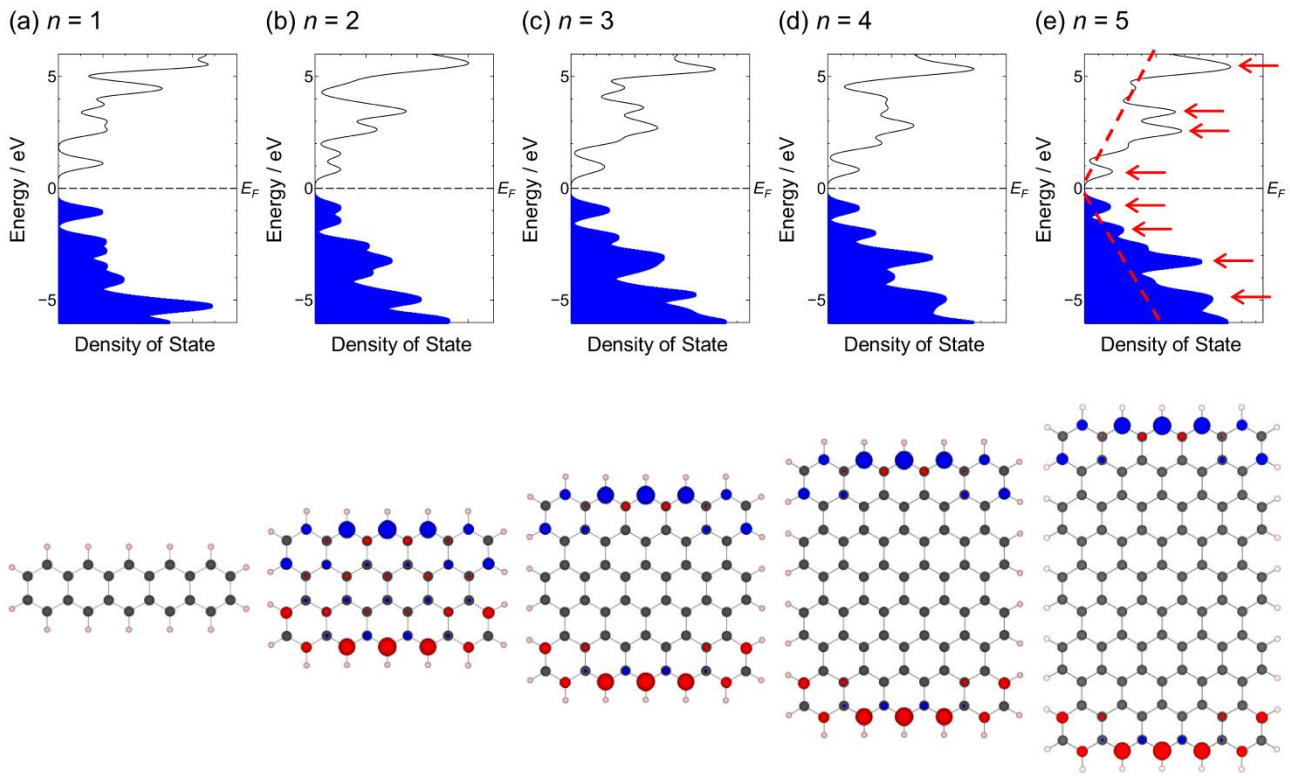

Fig. 3 Electronic density of states plots (DOS, upper) and graphical representation of net spin densities (lower) of (a) pentacene, (b) peripentacene, (c) trisperipentacene, (d) tetrakisperipentacene, and (e) pentakisperipentacene calculated by the spin-unrestricted B3LYP/cc-pVDZ method. The DOS plots were obtained as the sum of Gaussian functions centered at molecular orbital energies with a full width at half maximum of 0.5 eV. In these figures, the positions of Fermi energies (E_F) are set as 0 eV and valence levels are filled with blue. In the spin density plots, red and blue regions represent excess α-spin density and excess β-spin density, respectively.

The fused pentacenes (n > 2) also seem to have unique magnetic properties. Although the net electronic structures of the fused pentacenes have been described as a singlet, their α- and β-spin densities were asymmetrically located at two opposing

zigzag edges (see Fig. 3). Similar asymmetrical spin features have been theoretically predicted for GNRs and SWCNTs having a zigzag edge structure[28-30, 32, 52,] but such a unique feature was not observed in the initial pentacene precursor (n = 1). Interestingly, the unique spin feature also seems to exist in other GNFs having acene monomer units larger than anthracene (see Fig. S6[†]). Such a localized spin feature should be favourable for magnetic applications. The obtained fused pentacenes may be used as a model material for studying the electromagnetic properties of spin-localized GNFs.

Because of the existence of various molecules and isotope ions, the observed mass spectra were highly complicated. To evaluate the detailed molecular distributions of the mass spectra, we performed spectrum analysis that considered isotope distribution. Strictly speaking, we cannot discuss the exact quantitative distributions in the entire range of the spectra owing to differences in the ionization efficiency of molecules. However, the discussion of individual band regions should be meaningful. This is because the ionization efficiencies of molecules in the same region should be similar owing to their similar elemental composition, structure, and molecular weight. The simulation patterns were calculated as the sum of isotope patterns of various hydrocarbon molecules (C_aH_b, a, b = 1, 2, 3$\cdots$). The peak intensities of the isotope patterns were sequentially fitted to those of the observed patterns in the order of increasing molecular weight. Here, we did not consider the existence of multivalent ions because every observed mass peak was separated at constant intervals of 1 mass unit. The simulated patterns of each region are shown in Fig. 2(b). It can be seen that the simulated patterns reproduced the observed spectra well only by assuming $C_{22n}H_{14n-2x}$ (x = 0, 1, 2, 3$\cdots$) type molecules. This result indicates that pentacene (**1**, $C_{22}H_{14}$) molecules were polymerized with a stepwise elimination reaction of H_2 molecules.

As mentioned before, straightly grown products (**4**) are expressed as $C_{22n}H_{4n+10}$. Other observed peaks having a larger number of hydrogen atoms ($C_{22n}H_{4n+12}$, $C_{22n}H_{4n+14}$, $C_{22n}H_{4n+16}\cdots$) can be explained by the relative positioning of the two pentacene units (i.e., shift) and/or unconnected sites as in structures **5**, **6**, and **7** shown in Fig. 4. In addition, molecules having smaller number of hydrogen atoms than that of the straightly grown products (**4**), such as $C_{22n}H_{4n+8}$, and $C_{22n}H_{4n+6}$, were also detected in this study. These hydrogen-poor molecules were not mentioned in the previous reports, but the structure of these molecules might be explained by the five-member ring structure included at shifted sites such as **8**. By introducing the five-member ring, steric repulsions between hydrogen atoms placed at the shifted sites (marked with circles in Fig. S7[†]) should be weakened.

Until now, we have focused on purified samples (i.e., fused components that are insoluble in toluene). Let us broaden our scope to soluble byproducts that were removed in the purification process. A typical LDI-TOF mass spectrum of a soluble component recovered in the purification process is shown in Fig. 5. As shown in the figure, the molecules in the soluble component have greater molecular weight than those in the insoluble component. Through a detailed spectrum analysis, we found that this difference in molecular weight is explained by the different number of hydrogen atoms in the structures; although the number of carbon atoms in each component was the same, the molecules in the soluble component contained more hydrogen atoms than the insoluble component. As clearly shown in Fig. 5, such hydrogen-rich molecules were well removed in the purification process. We found that except for toluene, the hydrogen-rich molecules showed higher solubility in commonly used organic solvents (such as cyclohexane and tetrahydrofuran) compared with the hydrogen-poor products. This is probably owing to the electric dipole moments of the hydrogen-rich molecules originating from the intricate three-dimensional structure in contrast to the planer structure of well-dehydrogenated graphene-like fragments. Toluene liquids containing hydrogen-rich molecules (soluble components removed in the purification process) were yellow or red; on the other hand, the recovered hydrogen-poor insoluble components (purified FPs) were black. These results indicate that conjugated carbon systems of the hydrogen-rich molecules were not well developed in contrast to the hydrogen-poor molecules. Note that as far as we tested, the hydrogen-poor molecules (purified FPs) did not dissolve in any solvent except 1-methyl-2-pyrrolidinone (NMP). Interestingly, the purified FP samples that dissolved in NMP showed intense blue photoluminescence under 365 nm ultraviolet light exposure (see Fig. S8[†]). The observed luminescence phenomenon may reflect the unique electronic structure of fused pentacene molecules. As is well known, bulk graphene does not show such photoluminescence because of its simple semi-metallic energy structure. On the other hand, fused pentacenes are expected to have some band gap and discrete energy levels probably caused by the quantum-size or edge effect as discussed above. This discrete energy structure of the fused pentacene system might work as a luminescent centre.

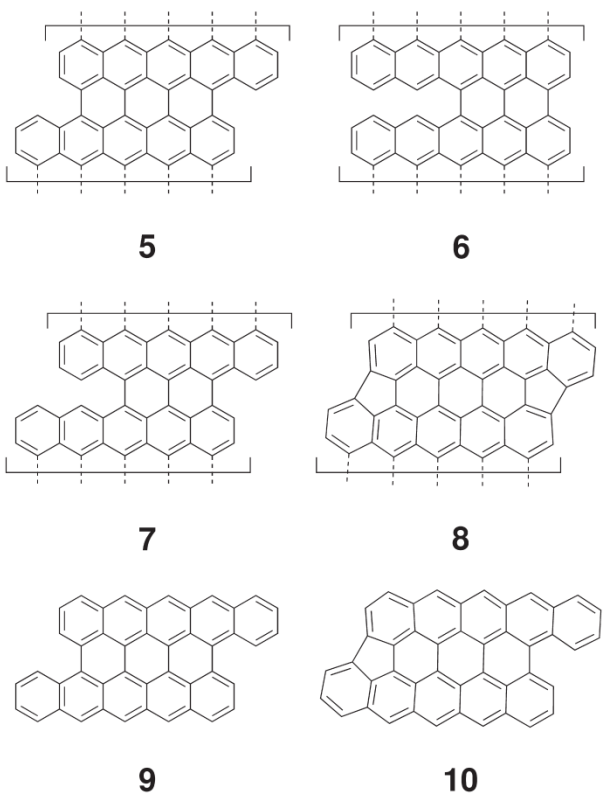

Fig. 4 Possible structure of byproducts included in the obtained materials.

Although the hydrogen-rich molecules observed in the soluble components are undesirable byproducts for the synthesis of nanosize graphene-like molecules, we can acquire useful information about the reaction mechanism from these molecules. Here, we would like to address the fusing mechanism of pentacene molecules. In a previous report, Northrop *et al.* discussed the formation mechanism of peripentacene (**2**) from a theoretical view point.[53] However, to the best of our knowledge, no experimental verification was performed after Northrop's report. Therefore, we attempt to discuss it here on the basis of mass spectroscopic analysis.

In the LDI-TOF mass spectra of the soluble components (Fig. 5), some molecules having hydrogen atoms larger than 14*n* at the *n*'th-mer region (such as $C_{22n}H_{14n}$, $C_{22n}H_{14n+2}$, and $C_{22n}H_{14n+4}$) were observed. These hydrogen-rich molecules cannot be explained by the fused products generated only by the dehydrogenation reactions. This is because such dehydrogenated products should be expressed as $C_{22n}H_{14n-2x}$, where *x* is the number of sublimated hydrogen molecules. This means that some types of hydrogen-atom-addition or hydrogen-atom-transfer reactions also occurred in the reaction tubes. According to the previous report, these hydrogen-rich molecules seem to be attributed to the reaction intermediates produced within the fusion process. In the reaction pathway proposed by Northrop *et al*., the 6-hydropentacenyl radical ($C_{22}H_{15}^{\cdot}$, **6PR**) was treated as a requisite intermediate.[53] They claimed that once **6PR** was generated, $C_{44}H_{30}$ (**11**) and the radical $C_{44}H_{29}^{\cdot}$ (**12**) were easily produced by the dimerization reaction of **6PR**s (Scheme 2a) and the addition reaction of **6PR** and **1** (Scheme 2b), respectively. Then, **11** and **12** are gradually converted to a peripentacene (**2**) through a dehydrogenation process. Based on this mechanism, the peak observed at *m*/*z* = 558.24 in Fig. 5 seems to be attributed to **11** (*m* = 558.23). Except for $C_{44}H30$ (**11**), the existence of $C_{44}H_{24}$, $C_{44}H_{26}$, $C_{44}H_{28}$, $C_{44}H_{32}$, and $C_{44}H_{34}$ was also confirmed in the soluble component (Fig. S9†). The observed $C_{44}H_{24}$, $C_{44}H_{26}$, and $C_{44}H_{28}$ molecule can be explained by dehydrogenated product **11**. The other molecules were not fully discussed in the previous report, but we think that the molecules can also be explained by the additional hydrogen-atom addition/transfer reaction of **11** and **12**. Because the radical species generated in the dimerization process (such as **12**, **6PR**, and **13**) are expected to have high reactivity, various types of side reactions (*e.g.*, hydrogen-atom abstraction, hydrogen-atom transfer) are conceivable.

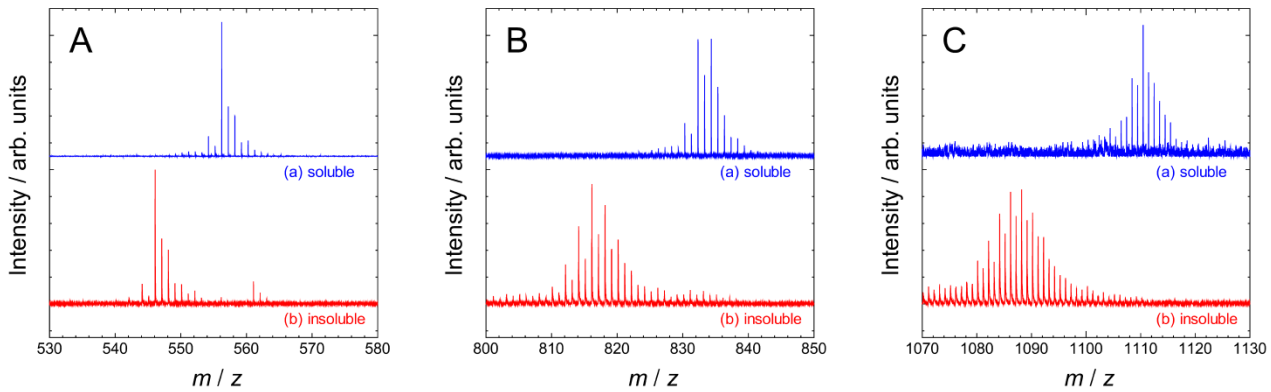

Fig. 5 LDI-TOF mass spectra of the FP-30-325 sample. The soluble components that were removed in the purification process (a) and the purified component that was insoluble in toluene (b) are compared. Magnified views of the dimer (*n* = 2), trimer (*n* = 3), and tetramer (*n* = 4) regions are separately shown in A, B, and C, respectively.

An important issue is the origin of **6PR**. Although the de-tailed reaction pathway was somewhat different from that in Northrop's report, the formation of **6PR** was also predicted in the Roberson's report.[38] In both reports, the assumption was that **6PR** was generated from the radical-type hydrogen-atom transfer from **DHP** to pentacene (**1**) at the initial reaction step (Scheme 2c).[38, 53] Here, **DHP** was treated as a trace amount of impurity that is often contained in commercially available pentacenes. However, we found that the precursor used in this study did not contain any **DHP** impurity (see Fig. S10†). In addition, **DHP** (*m* = 280.13) was not observed in treatment below 325 °C as shown in Fig. S11†. This indicates that the initial polymerization reaction should occur without a **DHP** molecule. Because the initial pentacene sample used in this study did not contain any organic and metallic impurity (see Figs. S10† and S12†), we believe that a disproportional reaction of two pentacene molecules (Scheme 2d) should have occurred without a catalyst at the first step. Even through Scheme 2d, **6PR** can be produced from the reaction route of **DHP** and pentacene (Scheme 2c). In addition, by considering Scheme 2d, additional simple dimerization routes, such as Scheme 2f, can also be considered in addition to previously discussed Schemes 2a and 2c. The reaction root shown in Scheme 2d is probably high-energy unfavourable process compared to the Scheme 2c. However, once **6PR** is generated through Scheme 2d, **DHP** can be produced from **6PR** through a backward reaction of Scheme 2c and a hydrogen-atom abstraction reaction of Scheme 2e. Thus, the difference between Schemes 2c and 2d becomes unclear after initial radical formation. To check the role of the **DHP** molecule more actively, experiments using **DHP** mixed with the initial pentacene precursor were performed. The obtained LDI-TOF mass spectra are summarized in Fig. S13†. As shown in the figure, the addition of DHP molecules did not promote fusing reactions. This result also supports our initial DHP-free reaction mechanism.

As mentioned above, the electronic structure of fused pentacene molecules is almost independent of the polymerization degree (see Fig. 3). Because reactive zigzag edge structures remain even through fusing reactions, additional fusion can occur.

Therefore, the formation mechanism of large fused pentacenes (trimer, tetramer, pentamer⋯) might also be explained by the further addition reaction of radical-activated pentacene (**6PR**, **13**) molecules.

Finally, we would like to discuss the suitable reaction conditions for obtaining large fused pentacenes based on the above-mentioned reaction mechanism. We investigated the effect of reaction temperature and initial precursor weight in this study. As a result, the lowest reaction temperature (T_{low}) required for the fusing reaction was found to be 310 °C < T_{low}< 325 °C. Above 325 °C, the relative abundances of highly polymerized products gradually decreased with increasing reaction temperature (see Fig. 1). In addition, we found that the molecular distributions of fused products broadened with increasing reaction temperature (see Fig. S11†). These results probably came from the low selectivity of the fusing reaction. The regioselectivity of the pentacene dimerization process was discussed in the previous theoretical study.[53] Although formation of straightly grown pentacene (such as **2**) is energetically the most preferable process compared with shifted ones (such as **9**), the energy difference does not seem to be very large in some cases. Because the fusing reaction of pentacenes can be explained by radical reactions via unstable intermediates such as **6PR** and **13**, various types of side reactions can be considered and the final byproducts became ignorable especially at high temperature conditions. The observed large distribution of fused molecules at high temperature might have occurred because the emergence of side-reaction pathways and byproducts is unfavourable for obtaining large fused pentacenes. This is because the relative formation probability of valid fused products should be decreased in a statistical sense. Moreover, initial precursor weight also affected the efficiency of the fusing reaction. As far as we tested, the most suitable initial pentacene weight was found to be about 30 mg for a 20 cm^3 quartz tube (see Fig. S2†). We think that this result can be explained by the inner gas pressure of the reaction tube. As the important intermediates for the fusing reaction (such as **6PR** and **13**) are generated by gas-phase bimolecular reactions, as shown in Scheme 2d, a certain amount of vapour pressure in initial pentacene is required for bimolecular collision. In this sense, a larger amount of initial pentacene is more suitable for promoting the fusing reaction. On the other hand, excess gas pressure accompanied by an excessive amount of initial pentacene in the reaction tube is also unfavourable because hydrogen-gas eliminations accompanied by the fusing reactions should be suppressed. Based on the balance of these conflicting factors, the optimal precursor value seemed to be 30 mg.

Cite this: DOI: 10.1039/c0xx00000x

www.rsc.org/xxxxxx

ARTICLE TYPE

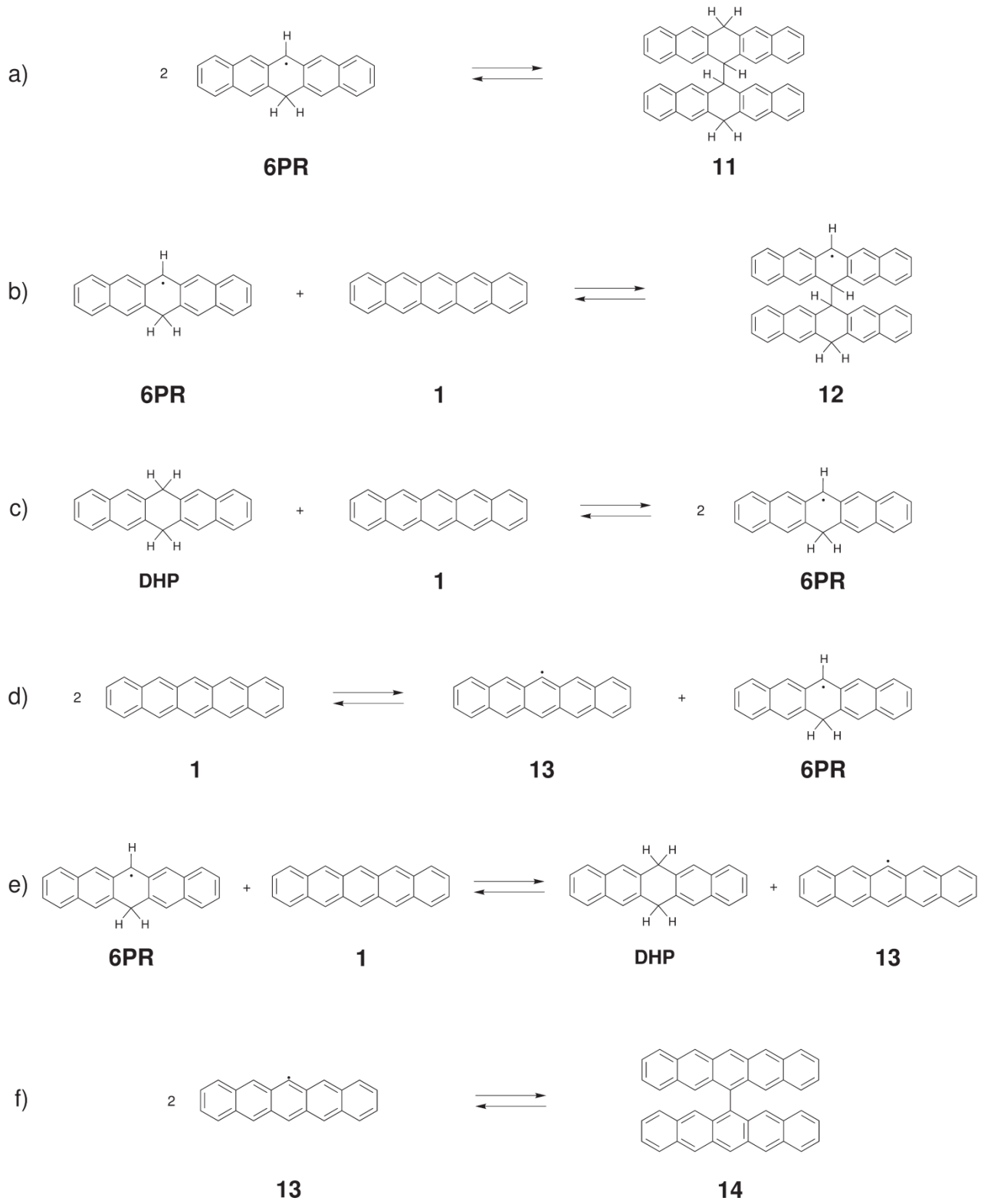

Scheme 2 Possible dimerization process of pentacene and related molecules.

Conclusions

We investigated the synthesis condition and products of a polymerized pentacene system. By optimizing the fusing condition, we have successfully obtained large fused pentacene molecules up to at least octamer (n = 8). First-principles calculations revealed that the fused pentacenes have a unique electronic structure that does not exist in bulk graphene samples. To evaluate the reaction mechanism, detailed mass spectroscopical analysis was performed. The fusing mechanism of pentacene molecules seems to be explained by a complex radical reaction pathway via the **6PR** intermediate as mentioned in previous studies. However, our perspective of the **6PR** formation scheme was somewhat different from the previous report; we think that **6PR** was formed without the **DHP** impurity at the initial step. Although various lengths of fused pentacenes were confirmed through mass spectra, the synthesized materials were obtained as a "mixture." To study more detailed physical properties of the fused systems, a separation method should be developed as the next step. Fortunately, various separation methods have been proposed for nanocarbon systems (especially for SWCNTs) and the technique is still being developed.[54–57] We expect that separation of pentacene-polymer will be possible in the near future.

Notes and references

[a] *Department of Materials Science and Engineering, Nagoya Institute of Technology, Gokiso-cho, Showa-ku, Nagoya 466-8555, Japan. Fax: +81 52-735-5221; Tel: +81 52-735-5221; E-mail: kawasaki.shinji@nitech.ac.jp*

[b] *Kuroganekasei Co. Ltd., 87 Arajingiri, Nishinaka, Chiryu 472-0016, Japan.*

† Electronic Supplementary Information (ESI) available: Characterization methods. Unit cell structure of the pentacene-based GNR used for the calculation. LDI-TOF mass spectra compared with initial pentacene weight. Raman spectrum of the FP-30-325 sample. XRD pattern of the FP-30-325 sample. DOS and spin-density plots of GNFs having various monomer widths. Band structure and DOS of pentacene-based GNR. Graphical representations of steric repulsions between hydrogen atoms placed at the shifted site. Photoluminescent spectrum of the FP-30-325 sample dissolved in NMP. LDI-TOF mass spectra (dimer region) of the soluble component of the FP-30-325 sample. LDI-TOF mass spectrum of the initial pentacene sample used for the fusing reaction. Detailed LDI-TOF mass spectra compared with heat treatment temperature. Energy-dispersive X-ray (EDX) spectrum of the initial pentacene sample used for the fusing reaction. LDI-TOF mass spectra compared with the initial pentacene/DHP ratio. See DOI: 10.1039/b000000x/

1 K. S. Novoselov, A. K. Geim, S. V. Morozov, D. Jiang, Y. Zhang, S. V. Dubonos, V. Grigorieva, and A. A. Firsov, *Science* 2004, **306**, 666-669.

2 A. K . Geim, and K. S. Novoselov, *Nat. Mater.* 2007, **6**, 183-191.

3 M. I. Katsnelson, *Mater. Today*, 2007, **10**, 20-27.

4 A. K. Geim, *Science* 2009, **324**, 1530-1534.

5 C. N. R. Rao, A. K. Sood, K. S. Subrahmanyam,and A. Govindaraj, *Angew. Chem. Int. Ed.* 2009, **48**, 7752-7777.

6 F. Schwierz, *Nat. Nanotechnol.* 2010, **5**, 487-496.

7 F. Schedin, A. K. Geim, S. V. Morozov, E. W. Hill, P. Blake, and M. I. Katsnelson, *Nat. Mater.* 2007, **6**, 652-655.

8 R. K. Joshi, H. Gomez, F. Alvi, and A. Kumar, *J. Phys. Chem. C* 2010, **114**, 6610-6613.

9 Y. Shao, J. Wang, H. Wu, J. Liu, I. Aksay, and Y. Lin, *Electroanalysis* 2010, **22**, 1027-1036.

10 W. Yang, K. R. Ratinac, S. R. Ringer, P. Thordarson, J. J. Gooding, and F . Braet, *Angew. Chem. Int. Ed.* 2010, **49**, 2114-2138.

11 K. S. Kim, Y. Zhao, H. Jang, S. Y. Lee, J. M. Kim, K. S. Kim, J. -H. Ahn, P. Kim, J. -Y. Choi, and B. H. Hong, *Nature* 2009, **457**, 706-710.

12 G. Kalita, M. Matsushima, H. Uchida, K. Wakita, and M. Umeno, *J. Mater. Chem.* 2010, **20**, 9713-9717.

13 E. J. Yoo, J. Kim, E. Hosono, H. -S. Zhou, T. Kudo, and I. Honma, *Nano Lett.* 2008, **8**, 2277-2282.

14 M. D. Stoller, S. Park, Z. Yanwu, J. An, and R. S. Ruoff, *Nano Lett.* 2008, **8**, 3498-3502.

15 C. Wang, D. Li, C. O. Too, and G. G. Wallace, *Chem. Mater.* 2009, **21**, 2604-2606.

16 D. Pan, S. Wang, B. Zhao, M. Wu, H. Zhang, Y. Wang, and Z. Jiao, *Chem. Mater.* 2009, **21**, 3136-3142.

17 C. Berger, Z. Song, T. Li, X. Li, A. Y. Ogbazghi, R. Feng, Z. Dai, N. Alexei, M. E. H. Conrad, P. N. First, and W. A. De Heer, *J. Phys. Chem. B* 2004, **108**, 19912-19916.

18 C. Berger, Z. Song, X. Li, X. Wu, N. Brown, C. Naud, D. Mayou, T. Li, J. Hass, A. N. Marchenkov, E. H. Conrad, P. N. First, and W. A. De Heer, *Science* 2006, **312**, 1191-1196.

19 H. Huang, W. Chen, S. Chen, and A. T. S. Wee, *ACS Nano* 2008, **2**, 2513-2518.

20 K. V. Emtsev, A. Bostwick, K. Horn, J. Jobst, G. L. Kellogg, L. Ley, J. L. McChesney, T. Ohta, S. A. Reshanov, J. Röhrl, E. Rotenberg, A. K. Schmid, D. Waldmann, H. B. Weber, and T. Seyller, *Nat. Mater.* 2009, **8**, 203-207.

21 P. W. Sutter, J. -I. Flege, and E. A. Sutter, *Nat. Mater.* 2008, **7**, 406-411.

22 X. Li, W. Cai, L. Colombo, and R. S. Ruoff, *Nano Lett.* 2009, **9**, 4268-4272.

23 Y. Zhang, L. Gomez, F. N. Ishikawa, A. Madaria, K. Ryu, C. Wang, A. Badmaev, and C. Zhou, *J. Phys. Chem. Lett.* 2010, **1**, 3101-3107.

24 H. Zhang, and P. X. Feng, *Carbon* 2010, **48**, 359-364.

25 A. T. T. Koh, Y. M. Foong, and D. H. C. Chua, *Diam. Relat. Mater.* 2012, **25**, 98-102.

26 K. Nakada, M. Fujita, G. Dresselhaus, and M. S. Dresselhaus, *Phys. Rev. B* 1996, **54**, 17954-17961.

27 Y. -W. Son, M. L. Cohen, and S. G. Louie, *Phys. Rev. Lett.* 2006, **97**, 216803.

28 Y. -W. Son, M. L. Cohen, and S. G. Louie, *Nature* 2006, **444**, 347-349

29 V. Barone, O. Hod, and G. E. Scuseria, *Nano Lett.* 2006, **6**, 2748-2754.

30 L. Pisani, J. A. Chan, B. Montanari, and N. M. Harrison, *Phys. Rev. B* 2007, **75**, 064418.

31 C. D. Simpson, J. D. Brand, A. J. Berresheim, L. Przybilla, H. J. Räder, and K. Müllen, *Chem.-Eur. J.* 2002, **8**, 1424-1429.

32 A. V. Talyzin, S. M. Luzan, K. Leifer, S. Akhtar, J. Fetzer, F. Cataldo, Y. O. Tsybin, C. W. Tai, A. Dzwilewski, and E. Moons, *J. Phys. Chem. C* 2011, **115**, 13207-13214.

33 A. Chuvilin, E. Bichoutskaia, M. C. Gimenez-Lopez, T. W. Chamberlain, G. A. Rance, N. Kuganathan, J. Biskupek, U. Kaiser, and A. N. Khlobystov, *Nature Mater.* 2011, **10**, 687–692.

34 T. W. Chamberlain, J. Biskupek, G. A. Rance, A. Chuvilin, T. J. Alexander, E. Bichoutskaia, U. Kaiser, and A. N. Khlobystov, *ACS Nano* 2012, **6**, 3943–3953.

35 A. V. Talyzin, I. V. Anoshkin, A. V. Krasheninnikov, R. M. Nieminen, A. G. Nasibulin, H. Jiang, and E. I. Kauppinen, *Nano Lett.* 2011, *11*, 4352-4356.

36 A. N. Khlobystov, *ACS Nano* 2011, **5**, 9306-9312.

37 J. Cai, P. Ruffieux, R. Jaafar, M. Bieri, T. Braun, S. Blankenburg, M. Muoth, A. P. Seitsonen, M. Saleh, X. Feng, K. Müllen, and R. Fasel, *Nature* 2010, **466**, 470-473.

38 L. B. Roberson, J. Kowalik, L. M. Tolbert, C. Kloc, R. Zeis, X. Chi, R. Fleming, and C. Wilkins, *J. Am. Chem. Soc.* 2005, **127**, 3069-3075.

39 Y. Ishii, T. Sakashita, S. Kawasaki, H. Kato, and M. Takatori, *Mater. Express* 2011, **1**, 36-42.

40 M. J. Frisch, G. W. Trucks, H. B. Schlegel, G. E. Scuseria, M. A. Robb, J. R. Cheeseman, J. A. Montgomery Jr., T. Vreven, K. N. Kudin, J. C. Burant, J. M. Millam, S. S. Iyengar, J. Tomasi, V. Barone, B. Mennucci, M. Cossi, G. Scalmani, N. Rega, G. A. Petersson, H. Nakatsuji, M. Hada, M. Ehara, K. Toyota, R. Fukuda, J. Hasegawa, M. Ishida, T. Nakajima, Y. Honda, O. Kitao, H. Nakai, M. Klene, X. Li, J. E. Knox, H. P. Hratchian, J. B. Cross, V. Bakken, C. Adamo, J. Jaramillo, R. Gomperts, R. E. Stratmann, O. Yazyev, A. J. Austin, R. Cammi, C. Pomelli, J. W. Ochterski, P. Y. Ayala, K. Morokuma, G. A. Voth, P. Salvador, J. J. Dannenberg, V. G. Zakrzewski, S. Dapprich, A. D. Daniels, M. C. Strain, O. Farkas, D. K. Malick, A. D. Rabuck, K. Raghavachari, J. B. Foresman, J. V. Ortiz, Q. Cui, A. G. Baboul, S. Clifford, J. Cioslowski, B. B. Stefanov, G. Liu, A. Liashenko, P. Piskorz, I. Komaromi, R. L. Martin, D. J. Fox, T. Keith, M. A. Al-Laham, C. Y. Peng, A. Nanayakkara, M. Challacombe, P. M. W. Gill, B. Johnson, W. Chen, M. W. Wong, C. Gonzalez, and J. A. Pople, *Gaussian 03*, revision D.02; Gaussian, Inc.: Wallingford CT, 2004.

41 A. D. Becke, *J. Chem. Phys.* 1993, **98**, 5648-5652.

42 T. H. Dunning Jr., *J. Chem. Phys.* 1989, **90**, 1007-1023.

43 X. Gonze, B. Amadon, P. -M. Anglade, J. -M. Beuken, F. Bottin, P. Boulanger, F. Bruneval, D. Caliste, R. Caracas, M. Côté, T. Deutsch, L. Genovese, P. Ghosez, M. Giantomassi, S. Goedecker, D. R. Hamann, P. Hermet, F. Jollet, G. Jomard, S. Leroux, M. Mancini, S. Mazevet, M. J. T. Oliveira, G. Onida, Y. Pouillon, T. Rangel, G. -M. Rignanese, D. Sangalli, R. Shaltaf, M. Torrent, M. J. Verstraete, G. Zerah, and J. W. Zwanziger, *Computer Phys. Commn.* 2009, **180**, 2582-2615.

44 X. Gonze, G. -M. Rignanese, M. Verstraete, J. -M. Beuken, Y. Pouillon, R. Caracas, F. Jollet, M. Torrent, G. Zerah, M. Mikami, P. Ghosez, M. Veithen, J. -Y. Raty, V. Olevano, F. Bruneval, L. Reining, R. Godby, G. Onida, D. R. Hamann, and D. C. Allan, *Kristallogr.* 2005, **220**, 558-562.

45 J. P. Perdew, and Y. Wang, *Phys. Rev. B* 1992, **45**, 13244-13249.

46 P. E. Blöchl, *Phys. Rev. B* 1994, **50**, 17953-17979.

47 G. Kresse, and D. Joubert, *Phys. Rev. B* 1999, **59**, 1758-1775.

48 R. Juhasz, N. Elfström, and J. Linnros, *Nano Lett.* 2005, **5**, 275-280.

49 A. H. Castro Neto, F. Guinea, N. M. R. Peres, K. S. Novoselov, and A. K. Geim, *Rev. Mod. Phys.* 2009, **81**, 109-162.

50 S. -L. Li, H. Miyazaki, H. Hiura, C. Liu, and K. Tsukagoshi, *ACS Nano* 2011, **5**, 500-506.

51 R. Lv, and M. Terrones, *Mater. Lett.* 2012, **78**, 209-218.

52 A. J. Du, Y. Chen, G. Q. Lu, and S. C. Smith, *Appl. Phys. Lett.* 2008, **93**, 073101.

53 B. H. Northrop, J. E. Norton, K. and N. Houk, *J. Am. Chme. Soc.* 2007, **129**, 6536-6546.

54 M. Zheng, A. Jagota, E. D. Semke, B. A. Diner, R. S. McLean, S. R. Lustig, R. E. Richardson, and N. G. Tassi, *Nat. Mater.* 2003, **2**, 338–342.

55 R. Krupke, F. Hennrich, H. V. Löhneysen, and M. M. Kappes, *Science* 2003, **301**, 344–347.

56 T. Tanaka, H. Jin, Y. Miyata, and H. Kataura, *Appl. Phys. Express* 2008, **1**, 1140011–1140013.

57 Y. Feng, Y. Miyata, K. Matsuishi, and H. Kataura, *J. Phys. Chem. C* 2011, **115**, 1752–1756.